Polymer 53 (2012) 3642–3652

Contents lists available at SciVerse ScienceDirect

Polymer

journal homepage: www.elsevier.com/locate/polymer

Magnetic high density polyethylene nanocomposites reinforced with in-situ synthesized Fe@FeO core-shell nanoparticles

Qingliang He [a,b], Tingting Yuan [a], Jiahua Zhu [a], Zhiping Luo [c], Neel Haldolaarachchige [d], Luyi Sun [e], Airat Khasanov [f], Yutong Li [g], David P. Young [d], Suying Wei [b,**], Zhanhu Guo [a,*]

[a] Integrated Composites Laboratory (ICL), Dan F. Smith Department of Chemical Engineering, Lamar University, Beaumont, TX 77710, USA
[b] Department of Chemistry and Biochemistry, Lamar University, Beaumont, TX 77710, USA
[c] Microscopy and Imaging Center, and Materials Science and Engineering Program, Texas A&M University, College Station, TX 77843, USA
[d] Department of Physics and Astronomy, Louisiana State University, Baton Rouge, LA 70803, USA
[e] Department of Chemistry and Biochemistry, Texas State University—San Marcos, San Marcos, TX 78666, USA
[f] University of North Carolina at Asheville, Asheville, NC 28804, USA
[g] Magnetic Head Operation, Western Digital Corporation, Fremont, CA 94539, USA

ARTICLE INFO

Article history:
Received 19 April 2012
Received in revised form
1 June 2012
Accepted 5 June 2012
Available online 13 June 2012

Keywords:
Magnetic property
Rheology
Thermal stability

ABSTRACT

Magnetic high density polyethylene (HDPE) polymer nanocomposites (PNCs) with different loadings of iron@iron oxide core-shell nanoparticles (NPs) were fabricated by in-situ thermal decomposition of organometallic iron precursors in the HDPE-xylene solution. Attenuated total reflection-Fourier transform infrared spectroscopy (ATR-FTIR) measurement indicated that the HDPE chains were physically adsorbed onto the surface of NPs instead of forming chemical bonding during the formation of these PNCs. Transmission electron microscopy (TEM) micrographs revealed that the iron core NPs surrounded with iron oxide shell were formed in the HDPE hosting matrix with good dispersion, an inter-network structure was formed when the particle loading reached 10.0 wt%. Mössbauer spectrum analysis showed that the oxidization content of the iron NPs decreased with increasing the particle loading. The X-ray diffraction (XRD) analysis and differential scanning calorimetry (DSC) characterization demonstrated that the crystalline structure of HDPE matrix was not influenced by the incorporation of the NPs; however, fusion heat and crystalline fraction of the HDPE matrix decreased with the introduction of these NPs. The melt rheological behaviors were significantly changed as indicated by different complex viscosities, storage moduli and loss moduli between pristine HDPE and its PNCs. Magnetic property investigation revealed a soft ferromagnetic behavior for these HDPE PNCs at room temperature and the coercivity was decreased with increasing the particle loading. Thermal gravimetric analysis (TGA) demonstrated that the thermal stability of these HDPE PNCs was enhanced in the presence of the NPs. Dielectric properties of the HDPE PNCs were also investigated and discussed in detail.

1. Introduction

Magnetic polymer nanocomposites (PNCs) with unique physicochemical properties have been extensively explored by both academic scholars and industrial researchers. Magnetic properties can be obtained by incorporating magnetic elements such as iron [1,2], cobalt [3,4], and nickel [5,6] into the non-magnetic polymer matrix by either physical or chemical methods including in-situ polymerization [7,8], surface-initiated polymerization [9–14], solution blending [15–17], ball milling [8,18,19], surface wetting method [20], and ion exchange technique [21]. Physicochemical properties of these PNCs can be significantly improved through combining both the merits of the organic polymer matrix and the inorganic components with different nano-structures and sizes, including but not limited to magnetic property [18,20], dielectric property [22], thermal stability [23], mechanical property [24], and optical property [25,26]. The combination of these specific properties can be used for the potential development of multifunctional magnetic materials in many fields, such as microwave absorber [9,10], magnetic recording materials [27], energy storage devices [28], magnetic sensors [29], and drug delivery [30].

The most conventionally used magnetic element is iron [31]. Iron NPs have aroused extensive interests due to their magnetic

* Corresponding author. Tel.: +1 409 880 7654.
** Corresponding author. Tel.: +1 409 880 7976.
E-mail addresses: suying.wei@lamar.edu (S. Wei), zhanhu.guo@lamar.edu (Z. Guo).

0032-3861/$ – see front matter © 2012 Elsevier Ltd. All rights reserved.
http://dx.doi.org/10.1016/j.polymer.2012.06.010

and catalytic performances. Iron NPs with different sizes and structures can have enlarged coercivity compared with their bulk counterparts [32,33]. Iron NPs can be synthesized from soluble precursors in solutions through many methods including thermal [22,33] or sonochemical decomposition [34], and chemical reduction [6,35,36]. However, iron NPs tend to aggregate together due to the van der waals force, large specific surface area and high surface energy. Thus, how to efficiently and uniformly disperse NPs into the hosting polymer matrix becomes one of the major challenges in fabricating magnetic PNCs. In order to control the particle growth and dispersion, dispersant or surfactant was added during the formation of the NPs in solution [6,33,34]. For examples, Stöver et al. [33] fabricated magnetic polymer-Fe nanocomposites through a thermal decomposition of $Fe(CO)_5$ in the presence of ammonia and polymers (polyisobutylene, polyethylene, and polystyrene) grated with tetraethylenepentamine (TEPA). Several complicated steps were performed till the final fabrication of the polymer-Fe nanocomposites, i.e., polystyrene-based dispersants needed be prepared with either grafted or blocked with TEPA architectures; polyethylene-based dispersant was synthesized through polyethylene grafted maleic anhydride groups. Although these approaches can lead to well-dispersed polymer coated Fe nanocomposites, they are time-consuming and costly. Tannenbaum et al. [37] also used thermal decomposition of $Fe(CO)_5$ to form iron oxide nanoclusters (γ-Fe_2O_3) in polycarbonate/methylene chloride, polysulfone/methylene chloride, polystyrene/toulene, PMMA/toulene and poly(vinylidene difluoride)/N,N-dimethylformamide solutions. The synthesis process also consist several sophisticated steps, i.e., filtered $Fe(CO)_5$ was added drop wise into the polymer solution followed by vigorously mixing process; then the $Fe(CO)_5$/polymer solution was film cast onto sheets of glass to allow the evaporation of the solvent. Finally, thermal decompositions were carried out in a temperature-controlled vacuum oven with controlled atmosphere capability. Therefore, it is clear that magnetic polymer-iron PNCs can be fabricated through delicate steps with different types of polymer matrices in the presence of surfactant/dispersant. Without surfactant/dispersant, it is difficult to solve the particle dispersion issue.

Polyethylene (PE) is one of the most widely used thermoplastics. Among all types of PEs, high density polyethylene (HDPE) is a commonly used thermoplastic with high degree of crystalline structure [38–40]. Due to its low cost and energy consumption for processing, HDPE resin is ideal for many applications such as bags, bottles, films, and pipes [38]. Meanwhile, in comparison to other kinds of PEs, HDPE possesses higher tensile strength [41] attributed to its crystalline structure. Moreover, HDPE can effectively resist corrosions including moisture, acids/alkalis, and most of chemical solvents at room temperature. Organic clay [38], carbon nanotubes/nanofibers [40,42–45], and double layered hydroxides [46] are usually used to modify the thermal stability, flame retardancy, mechanical properties, and electrical conductivity of HDPE. Giri et al. had provided a special approach to prepare magnetic PE/Fe nanocomposites through direct ball milling PE and Fe powders in a sealed stainless steel container under inert atmosphere [47]. The Fe particle size was finally reduced approximately 4500 times from ~40 μm to ~9 nm due to the 200-h high energy ball milling process. The as-prepared nanocomposites have very high coercivity (~230 Oe of the Fe loading of 10%). This preparation of PE/Fe nanocomposites with good magnetic properties is very successful, and provides a new pathway to fabricate magnetic PE composites. Meanwhile, it is a time- and energy-consuming process with very sophisticated procedures, i.e., sealed container protected under argon. However, due to its rigid crystalline structure, HDPE has rarely been chosen to be the hosting polymer for metallic NPs. To our best knowledge, magnetic HDPE PNCs have not been reported and rarely studied.

In this work, magnetic HDPE PNCs were prepared through the in-situ thermal decomposition of $Fe(CO)_5$ in the refluxing xylene in presence of HDPE. Specifically, two facile steps were followed, i.e. dissolution of HDPE matrix in xylene followed by thermal decomposition of $Fe(CO)_5$ to form HDPE-iron PNCs with different particle loadings. HDPE acted as both hosting matrix and protecting agent to the in-situ formed iron NPs. This study is to provide a facile, fast, low-cost, one-pot, surfactant-free solution-based reaction approach to prepare magnetic HDPE/Fe@Fe_xO_y nanocomposites. It have been demonstrated that different morphology and physical property of these as-prepared nanocomposites can be prepared by only changing the polymer to metal precursor mole ratio. The synthesis condition is extremely mild, easy to control and repeat. The morphology of the NPs was investigated by TEM; the influences of the NPs on the HDPE were studied by XRD and DSC. Mössbauer spectrometer was used to disclose the valence state of iron in the formed PNCs. Thermal stability was investigated by TGA. Melt rheological behaviors, storage and loss modulus, magnetic properties and dielectric properties were also investigated.

2. Experimental

2.1. Materials

The HDPE used in this study was supplied by Total Petrochemicals USA Inc., with a density of 0.946 g/cm^3. Iron pentacarbonyl ($Fe(CO)_5$, 99%) was commercially obtained from Sigma Aldrich. Solvent xylene (laboratory grade, $\rho = 0.87$ g/cm^3) was purchased from Fisher Scientific. All the chemicals were used as-received without any further treatment.

2.2. Polymer nanocomposites fabrication

The brief procedures for preparing HDPE nanocomposites are as follow. Firstly, 9.0 g HDPE pallet and 100 ml xylene were added into a 250 ml three-neck round bottom flask; the mixture was heated to the boiling temperature of xylene (approximately 140 °C) and refluxed for 2 h in order to dissolve HDPE. After that, the solution was cooled down to around 120 °C, then 3.5 g $Fe(CO)_5$ was injected into the flask to obtain HDPE PNCs with a theoretical iron particle loading of 10 wt% (calculation was based on pure iron). The solution immediately turned from transparent to yellow and then gradually became black during the refluxing process for additional 3 h. The reflux speed was controlled at approximately 1–2 drops/sec in order to maintain the reaction smoothly taking place. Finally, the solution was cooled down to room temperature in the flask and then poured onto a large glass container to evaporate the solvent in the fume hood overnight. The black powders were collected and dried in a vacuum oven at room temperature for 24 h. Pure HDPE powders were also prepared as reference using the same procedures without adding $Fe(CO)_5$.

$Fe(CO)_5$ underwent a series of thermal decomposition reactions, released carbon monoxide under constant heating in HDPE-xylene solution, and finally formed the metallic NPs [22,48,49], which were simultaneously adsorbed to HDPE molecules. Oxidization took place on the surface of iron NPs and iron oxides were formed upon exposure to air.

The desired samples were prepared from the final powders (with different iron loadings in the HDPE matrix) using hot press molding machine (Model: Carver 3853-0, USA). The concise procedures are as follows. First, the powders were added into a cylinder-shaped mold and the mold was placed between the two panels in the molding machine. Second, the mold was heated to

180 °C at a heating rate of 20 °C/min under the pressure of 10 MPa; then maintained at 180 °C for an extra 5–10 min to ensure the formation of compact samples. Finally, the sample was cooled down to room temperature in the mold.

2.3. Characterization

The morphology of the HDPE PNCs was characterized by a transmission electron microscopy (TEM) with field emission gun, operated at an accelerating voltage of 200 kV. The samples from colloidal condition were prepared from the hot solution of HDPE PNCs by the end of fabrication process. One droplet of diluted hot solution containing the NPs was casted on a carbon film coated copper TEM grid. The solid sample was prepared by using microtome. First, a sample block was selected from the center part of the fabricated composites and trimmed to create a block face about 1 mm by 1 mm in size, then this block face was thin-sectioned to get about 70 nm thin slices using an Ultracut E ultramicrotome. The thin films were deposited on Cu grids. The samples are examined in TEM (FEI Tecnai G2 F20) at 200 kV, which was equipped with Gatan Image Filter for energy-filtering TEM (EFTEM) analysis.

Fourier transform infrared spectroscopy (FT-IR, Tensor 27, Bruker Inc.) with Hyperion 1000 ATR microscopy accessory was utilized to characterize the functional groups of pure HDPE and its PNCs over the wavenumber range of 4000 to 500 cm^{-1}.

X-ray diffraction (WAXD) analysis was carried out with a Bruker AXS D8 Discover diffractometer operating with a Cu Kα radiation source. The X-ray beam was generated at 40 kV and 27 mA power and XRD scans were recorded at 2θ from 6 to 60°.

The Mössbauer spectrometer was set to produce a high precision Doppler velocity modulation of the source γ radiation. The effects of the Doppler velocity modulation on the absorption of γ radiation were recorded synchronously in the 1024 channels of the multichannel analyzer. The result was 1024 numbers representing registered gamma quanta (representing a singular quantum) passing through the absorber under the condition of different Doppler velocity. A separate calibration procedure establishes the exact correspondence channel-velocity (Spectrometer calibration is performed by measuring a standard α-Fe absorber, which produces a well known six line spectrum. The whole velocity range is calibrated using these six velocity points). The shape of the absorption spectrum was fitted to a theoretical model line shape, which was a superposition of singlets, doublets and sextets (57Fe case) of a Lorentzian form. The result was investigated by chi 2 criterion and the theoretical line shape is tailored to fit experimental spectrum by the adjustment of spectral parameters like isomer shift, quadrupole splitting, hyperfine magnetic field and etc.

Differential scanning calorimetry (DSC) was carried out on a TA Instruments Q2000 calorimeter. Approximately 5 mg sample was encapsulated in an aluminum pan and heated from 0 to 250 °C at a heating rate of 10 °C/min under a nitrogen flow rate of 50 ml/min, then cooled down to room temperature after stayed at 250 °C for 3 min. After that, the samples were reheated again from room temperature to 250 °C. The data enclosed were collected from the first cooling and the second heating procedures in order to remove the heat history.

Thermal stability of the pristine HDPE and its PNCs were investigated using thermogravimetric analysis (TGA, TA Instruments Q-500). Samples were heated from room temperature to 700 °C at a constant heating rate of 20 °C/min under air and nitrogen gas atmosphere, respectively. The flow rate is 60 ml/min under both two atmospheres.

Melt rheological behaviors of HDPE matrix and its PNCs were studied using TA Instruments Rheometer (type AR 2000ex). Environmental test chamber (ETC) steel parallel-plate geometry (25 mm in diameter) was used to perform the measurements. A dynamic strain sweep at 1 rad/s was performed in order to find out the limit of linear viscoelasticity. Then, dynamic oscillation frequency was swept from 100 to 0.1 Hz in the linear viscoelastic range (LVR) with a strain of 1% at 200 °C under air atmosphere. The samples used are 25 mm in diameter with around 2 mm thickness prepared from hot press.

The magnetic property measurements of these PNCs were carried out in a 9 T physical properties measurement system (PPMS) by Quantum Design at room temperature.

Dielectric properties of pure HDPE and its PNCs were measured by an LCR meter (Agilent, E4980A) equipped with a dielectric test fixture (Agilent, 16451B) with frequency ranged from 20 to 2M Hz.The samples were the same size as the samples tested in the melt rheological measurements.

3. Results and discussion

3.1. TEM micrographs of colloidal solutions

Fig. 1(a–c) demonstrates the TEM micrographs of the HDPE PNCs containing 5.0, 10.0 and 20.0 wt% NPs under colloidal condition. With 5.0 wt% particle loading, the core-shell NPs were observed to be well dispersed with an average size of 5.5 $\pm$ 2.4 nm, Fig. 1a. When the particle loading increased to 10.0 wt%, the in-situ synthesized NPs in the hosting HDPE matrix still showed core-shell morphology with a slightly increased particle size of 6.7 $\pm$ 2.5 nm, Fig. 1b; and the dispersion quality was still good. However, a short curvy core-shell NP chain (in micron scale) and some aggregated core-shell NPs were observed when the particle loading reached 20.0 wt% in HDPE matrix under colloidal condition, Fig. 1c. The average particle size was further increased to 13.0 $\pm$ 4.0 nm. The Energy-filtered TEM (EFTEM) mapping can provide a 2-dimensional elemental distribution; thus, EFTEM is investigated here to further clarify the specific component of the core-shell NPs. The elemental map summation of iron (in red) and oxygen (in green) is shown in Fig. 1d. It is clear that the oxygen areas occupy the outside of iron, indicating the inner core as iron and the shell as oxygen.

In order to confirm whether or not the net-work particle microstructure still exists in the solid composite condition, the circular plate samples with 5.0, 10.0 and 20.0 wt% particle loadings (prepared from hot-press molding of the solid powders) had been taken to microtome to further investigate the TEM morphology. Fig. 2(a–c) shows the TEM images of these HDPE PNCs. With 5.0 wt% particle loading, the NPs had been observed distributed in the solid HDPE matrix with slightly agglomeration, Fig. 2a. When particle loading increased to 10.0wt%, the NPs in solid HDPE matrix were clearly found to aggregate into inter-connected structure (marked with yellow dash-line curves in Fig. 2b). Inter-network structure with large area agglomeration can be observed clearly when particle loading reached 20.0 wt% (marked with yellow dash-line curves in Fig. 2c). The elemental map summation of iron (in green) and oxygen (in red) is shown in Fig. 2d. It can be found that the green spots corresponding to iron were embedded into the red areas representing oxygen, indicating the inner core as iron and the shell as oxygen as these NPs aggregated. Thus, it can be concluded that the iron-iron oxide core-shell NPs became compact and formed inter-network in the HDPE matrix when the colloidal were dried into solid composites. The proposed mechanism of formation of different morphologies is depicted in Scheme 1.

Upon heating, $Fe(CO)_5$ went through a series of thermal decomposition and formed nanometer-sized metallic iron in the high temperature HDPE-xylene solution. HDPE molecules were adsorbed to and physically “wrapped” on the iron NPs through Van der waals forces. When particle distances were reduced with increasing

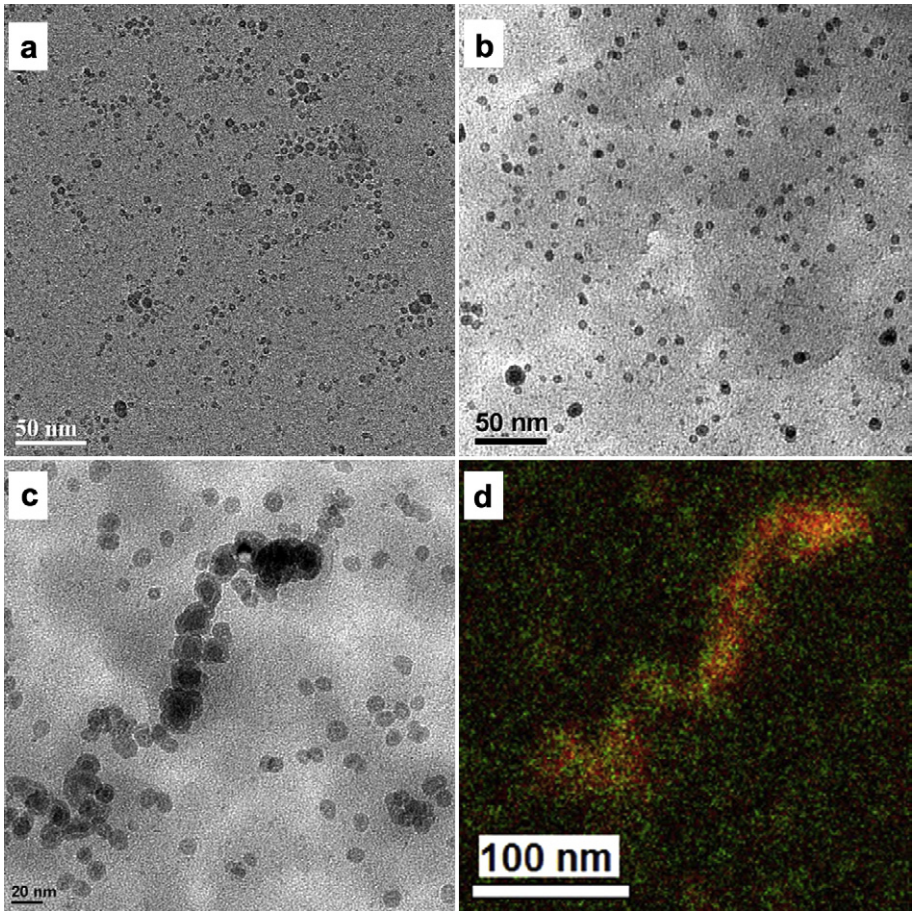

Fig. 1. TEM images of HDPE nanocomposites with a particle loading of (a) 5.0, (b) 10.0, (c) 20.0 wt%; and (d) iron-oxygen elemental mapping of HDPE PNCs with 20.0 wt% particle loading under colloidal condition.

particle loading, the remarkable magnetic dipolar-dipolar forces among these magnetic NPs are stronger than the repulsion forces from the wrapping HDPE backbone chains. Thus, the iron-iron oxide NPs tended to aggregate together in order to lower the high surface energy when the particle loading reached the critical point, which has usually been called as percolation threshold. Under colloidal condition, the strong magnetic dipolar interactions among the magnetic NPs are probably weakened by the solvent due to the larger volume of colloidal than the compact solid composites. This can explain the well dispersed NPs observed under colloidal condition; while aggregated NPs with inter-network structure were found in solid composite condition for HDPE PNCs with 10.0 wt% loading of NPs. Meanwhile, these "wrapped" HDPE layers were not solid enough to prevent oxygen from penetrating into the surface of iron; hence the surface of iron NPs was oxidized after the evaporation of solvent. The formed iron oxide shell can thus act as a shield to prevent the metallic iron core from further oxidization. The precise iron states in both the core and shell were further confirmed from Mössbauer spectra results below.

3.2. ATR-FTIR analysis

Fig. 3 depicts the FT-IR spectra of pure HDPE and its PNCs. For pure HDPE, there are two strong absorption peaks at approximately 2912 and 2846 cm^{-1}, corresponding to C–H symmetric and asymmetric stretching modes, respectively; and two C–H bending vibration absorption peaks at around 1462 and 718 cm^{-1} [50]. For all the PNCs incorporated with the in-situ synthesized NPs, the chemical structure of HDPE was well maintained as indicated by these unchanged characteristic peaks of HDPE matrix (Fig. 3). This suggests that the in-situ synthesized NPs were physically adsorbed by the HDPE molecules instead of forming chemical bonding during the synthesis process. It is worth noting that a new broad absorption peak at around 500–650 cm^{-1} is observed for all these HDPE PNCs, which corresponds to the vibration of Fe–O bond in Fe_2O_3 [51,52]. In addition, the peak strength becomes more intensive with increasing particle loading while negligible changes happened to the other absorption peaks, which is obviously due to the presence of more NPs in the hosting matrix.

3.3. XRD analysis

Fig. 4 shows the XRD patterns of the pristine HDPE and its PNCs. The pristine HDPE mainly exhibits a strong reflection peak at 21.6°, followed by a less intensive peak at 24.0°, which correspond to the typical orthorhombic unit cell structure of the (110) and (200) reflection planes, respectively. These 2θ values agree well with the reported values of polyethylene [38,53,54]. Two weak peaks at 2θ around 30.0 and 36.2° are corresponding to reflection planes (210) and (020), respectively [55,56]. In addition, there are several other weak reflection planes in the range of 38–44°, Fig. 4 [56]. The two characteristic crystalline peaks (planes 110 and 200) remained unchanged after the incorporation of the in-situ synthesized NPs, indicating that the addition of the NPs did not change the original crystal structure of HDPE matrix. Similar phenomena were also reported in the in-situ polymerized HDPE on the carbon nanotubes

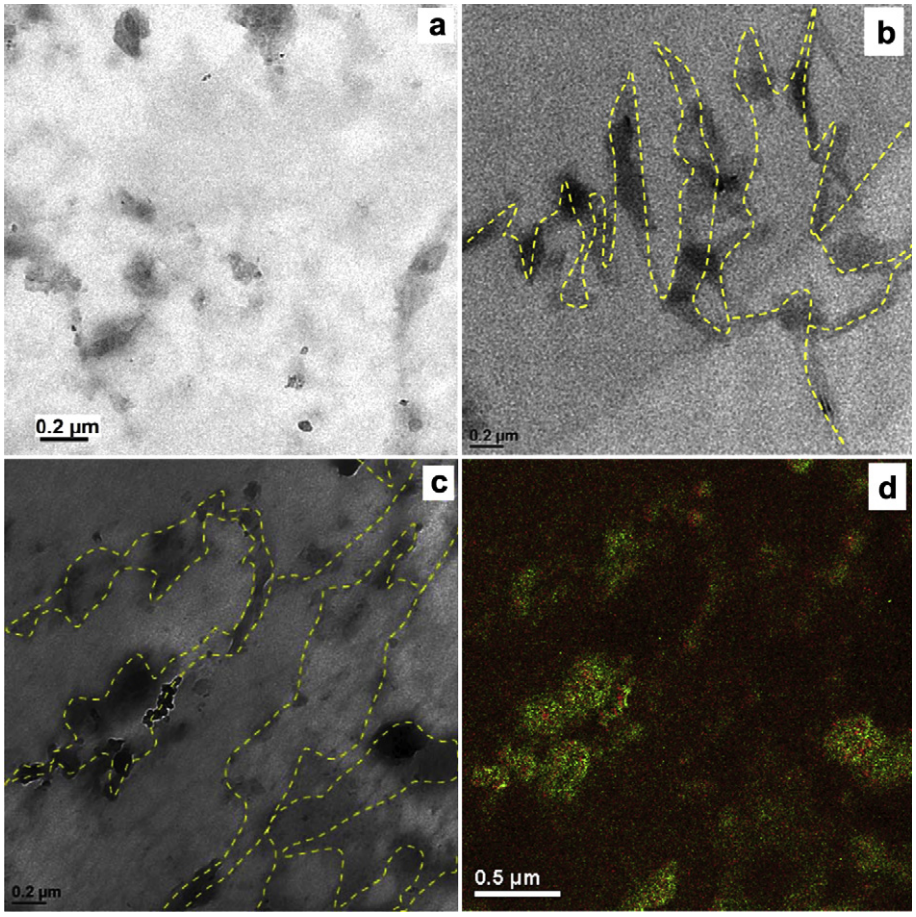

Fig. 2. TEM images of solid HDPE nanocomposites with a particle loading of (a) 5.0, (b) 10.0, (c) 20.0 wt%; and (d) iron-oxygen elemental mapping of HDPE PNCs with 20.0 wt% particle loading.

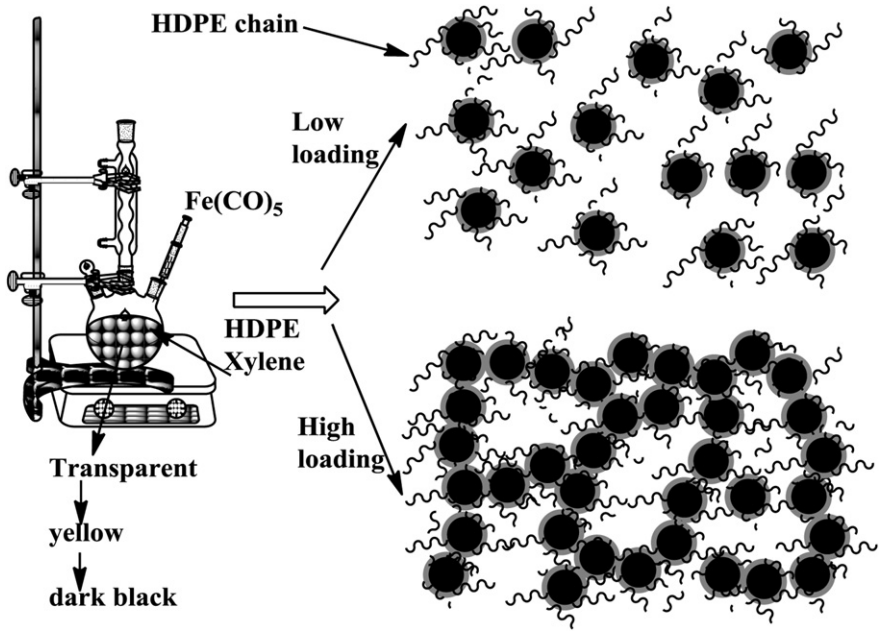

Scheme 1. Schematic formation of both dispersed and inter-connected structures in HDPE matrix.

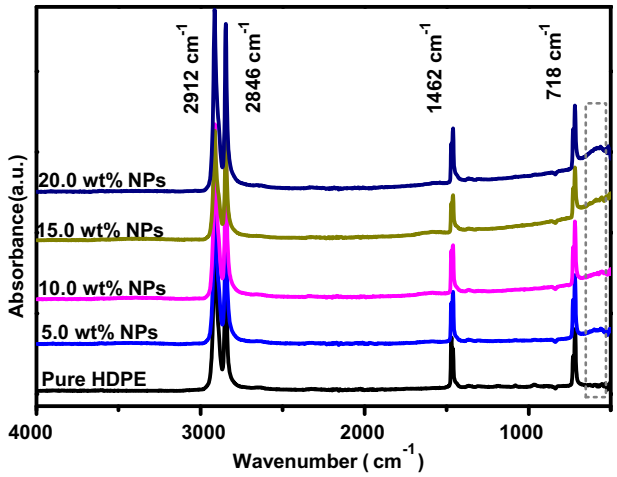

Fig. 3. FT-IR spectra of pure HDPE and its nanocomposites with different particle loadings.

[45] and HDPE-octamethyl POSS nanocomposites [57]. The relative intensity of these two peaks at 21.6 and 24.0° were attenuated with increasing the particle loading among all the HDPE PNCs, and these weak peaks at around 30–44° became even weaker. In addition, a small reflection peak at 2θ of 44.8° was clearly observed in the sample with 20.0 wt% particle loading, which corresponds to the metallic iron reflection [33,58]. Here, it is clear that little information was found from the XRD pattern for the iron NPs in our HDPE PNCs.

3.4. Mössbauer spectra measurements

In order to determine the precise species of the in-situ synthesized NPs in the hosting HDPE matrix, room temperature Mössbauer spectra of these as-prepared HDPE PNCs were investigated. In the case of HDPE/5.0 wt% NPs, Fig. 5a, the Mössbauer spectrum shows a main component (72%) at isomer shift (IS) of 0.41 mm/s and quadrupole splitting (QS) of 0.88 mm/s, which correspond to Fe^{3+} in a paramagnetic state in the distorted oxygen octahedral site. The second component is metallic iron (18%) as indicated by the other two symmetric peaks (IS = 0 mm/s, and H = 330 kOe). In addition, the final 10% iron is in Fe^{2+} state at low spin magnetic state (IS = 0.23 mm/s with H = 210 kOe).

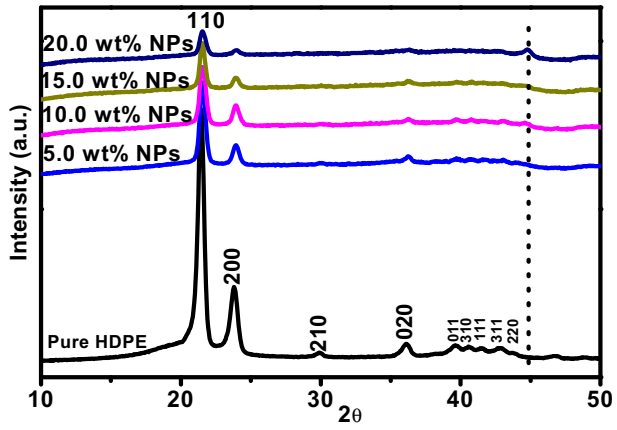

Fig. 4. X-ray diffraction patterns of HDPE and its nanocomposites with different particle loadings.

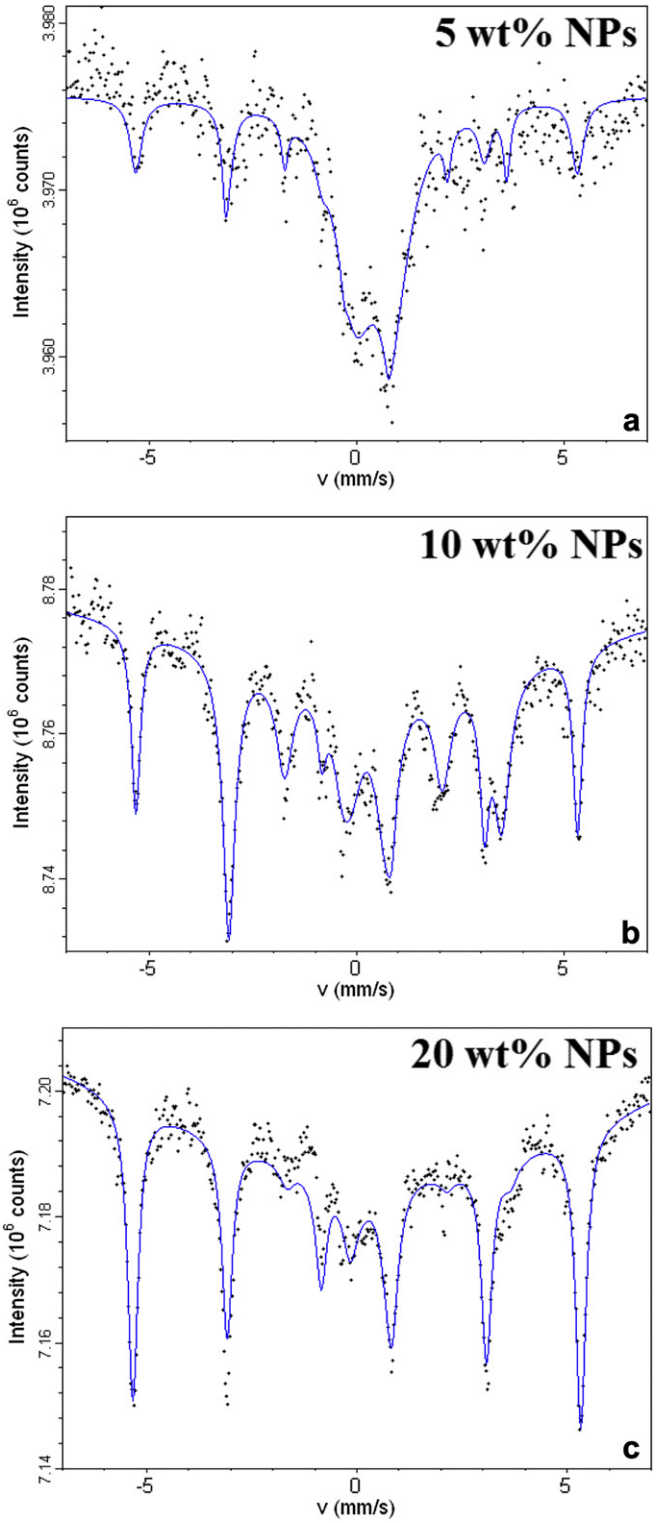

Fig. 5. Room temperature Mössbauer spectra of HDPE nanocomposites with a particle loading of (a) 5.0, (b) 10.0, and (c) 20.0 wt%, respectively.

When particle loading increased from 5.0 to 10.0 wt%, Fig. 5b, the metallic iron percentage increased from 18 to 32% (IS1 = 0 mm/s, H1 = 330 kOe); and Fe^{3+} decreased to 21% (IS2 = 0.28 mm/s, QS2 = 0.86 mm/s); meanwhile, Fe^{2+} in the low spin magnetic state increased to 47% (IS3 = 0.19 mm/s, H3 = 204 kOe). Similarly, the metallic iron further increased to 76% (IS1 = 0 mm/s, H1 = 330 kOe)

with particle loading increased to 20.0 wt%, Fig. 5c; and Fe^{3+} decreased to 13% (IS2 = 0.28 mm/s, QS2 = 0.86 mm/s); and Fe^{2+} decreased to 11% (IS3 = 0.18 mm/s, *H*3 = 204 kOe).

During the particle formation in the hosting matrix at a low particle loading, HDPE molecules adsorbed to the iron particle via weak interaction - Van der Waals forces. The particle growth can be restrained by these adsorbed long-chain molecules, hence restricting the particles from further growth [37]. When the particle loading increased, the reduced particle distance caused the small particles agglomerate to each other due to their high surface energy and large specific surface area. Therefore, the increased particle sizes and inter-network were observed from TEM images, Figs. 1 and 2, when particle loading increased. Hence, the possibility of oxygen penetrated to iron core can be relatively reduced, which is evidenced by the increased metallic iron percentage as revealed from Mössbauer spectra.

3.5. Differential scanning calorimetry (DSC)

Fig. 6(a,b) shows the DSC plots for the pristine HDPE and its PNCs and the detailed crystallization data (melting peak temperature, T_m; crystalline peak temperature, T_c; heat of fusion, ΔH_m; and crystalline fraction, F_c) are summarized in Table 1. The heat of fusion was directly integrated from the DSC curves. For 100% crystalline polyethylene, the best experimental heat of fusion is 4.1 kJ/mol of CH_2, which approximately equals to 293 J/g [59]. The crystalline fraction of pristine HDPE and its PNCs, F_c, was calculated from Equation (1):

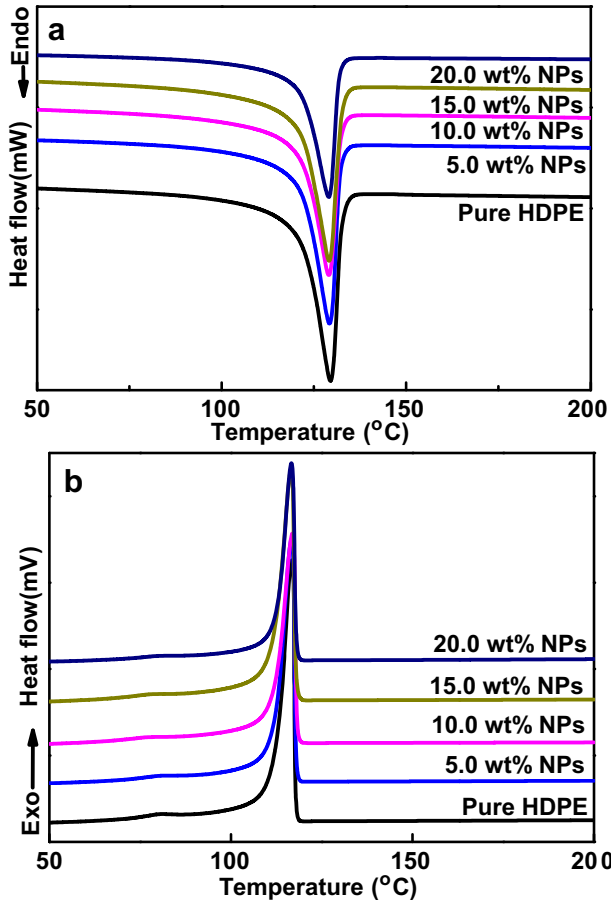

Fig. 6. DSC curves of pure HDPE and its nanocomposites: (a) 2nd heating and (b) 1st cooling cycles.

Table 1
DSC characteristics of the measured samples.

Composition	T_m (°C)	ΔH_m (J/g)	T_c (°C)	ΔH_c (J/g)	F_c (%)
Pure HDPE	129.8	181.8	116.7	169.3	62.0
5.0 wt% NPs	129.3	167.9	116.7	151.5	60.3
10.0 wt% NPs	129.3	157.2	116.7	139.1	59.6
15.0 wt% NPs	129.3	151.5	116.7	147.0	60.8
20.0 wt% NPs	129.3	140.9	116.7	126.7	60.1

$$F_c = \frac{\Delta H}{293 \times (1 - x)} \quad (1)$$

where, ΔH is the heat of fusion (J/g); 293 (J/g) is the fusion enthalpy for a theoretically 100% crystalline PE as mentioned above; and *x* is the loading of the NPs.

For the pristine HDPE, it demonstrates a T_m at 129.8 °C and a T_c at 116.7 °C. The F_c is 62.0% as calculated from Equation (1). It is obvious that all the PNCs show melting, Fig. 6a and crystalline peaks, Fig. 6b, the same as those of pure HDPE. These phenomena indicate that the original crystal structure of the hosting matrix remains unchanged in spite of the incorporation of the in-situ synthesized NPs. However, the F_c (Table 1) decreased slightly (3–4%) after the NPs were introduced into the hosting HDPE. The ΔH_m of HDPE decreased significantly from 181.8 to 167.9 J/g when 5.0 wt% NPs were incorporated in the HDPE matrix; and further decreased to 140.9 J/g in the PNCs with 20.0 wt% particle loading. As confirmed from XRD pattern, the crystalline structure of HDPE was not changed in all the PNC samples. Thus, the decrease of both XRD reflection peak intensity and the heat of fusion are probably due to the decrease in the crystalline size of HDPE molecules [22]. Upon heating in xylene, the HDPE molecular chains were relaxed and the NPs were formed among the relaxed HDPE chains. The lower F_c of these PNCs is attributed to the fact that the NPs are able to disturb the continuity of the HDPE chains and thus introduce more grain boundaries and defects in the hosting matrix; hence, the F_c was suppressed accordingly. Similar situations are also reported in the HDPE/carbon nanotube composites [60,61].

3.6. Thermogravimetric analysis (TGA)

Fig. 7(a,b) shows the TGA curves of pure HDPE and its PNCs under (a) nitrogen and (b) air atmosphere, respectively; and the detailed thermal decomposition temperatures are shown in Tables 2 & 3. Here, the initial (also called as onset) thermal decomposition temperature (T_{ini}) is defined as the temperature at 5% weight loss of the tested specimen; and $T_{50\%}$ is defined as the temperature at half weight loss of the tested specimen.

Under inert atmosphere, pure HDPE started to decompose at approximately 416.5 °C, and experienced a full decomposition at around 500 °C with little residue left (0.5%). For all HDPE PNCs incorporated with different particle loadings, the T_{ini} and $T_{50\%}$ were both increased, Fig. 7a and Table 2. With 20.0 wt% particle loading, the T_{ini} and $T_{50\%}$ increased to 432.0 and 469.0 °C, respectively. The final residues at 700 °C increased to 5.6, 10.3, 13.8 and 18.5% in the PNCs with a particle loading of 5.0, 10.0, 15.0 and 20.0 wt%, respectively. Since $Fe(CO)_5$ has a relatively high vapor pressure at room temperature [37], the slightly lower values in actual residues at high particle loadings are primarily due to the evaporation of some $Fe(CO)_5$ during the reflux process. It can be concluded that the thermal stability of the HDPE matrix was enhanced with the incorporation of the in-situ synthesized NPs.

TGA measurements under air atmosphere were used to investigate the influences of the iron/iron oxide NPs on the thermal

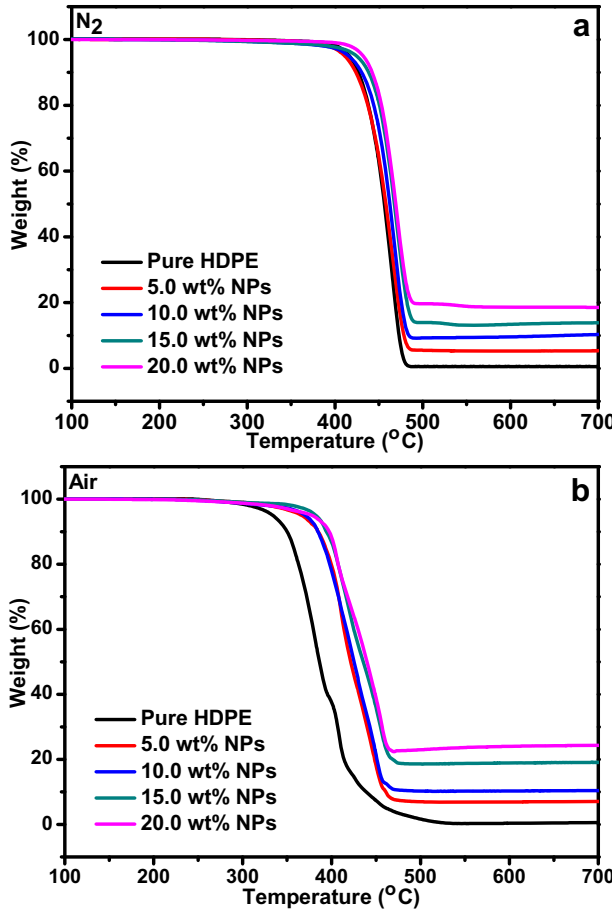

Fig. 7. TGA curves of pure HDPE and its nanocomposites under (a) nitrogen and (b) air.

oxidative degradation of the HDPE matrix. The pristine HDPE began to decompose at around 334 °C under air atmosphere, Fig. 7b, which was 82.5 °C ahead of its decomposition under inert atmosphere. It is obvious that the presence of oxygen significantly decreases the thermal stability of pure HDPE, which is apparently referred to the chemical composition of its main chains. HDPE chain can easily undertake oxygen insertion reaction when it was exposed to air at elevated temperatures, then it formed peroxy radical species and other oxidized species while the temperature was increased [62]. All these reactions weakened the thermal stability of the main chains of HDPE, which started to generate gaseous products under the air atmosphere at approximately 330 °C, thus leading the weight loss [62]. From 330 to around 510 °C, HDPE experienced a fast oxidative degradation till little residue (0.6%) left at 700 °C. The thermal oxidative degradation of the HDPE PNCs experienced differently compared with that of pure HDPE. First, with only 5.0 wt% particle loading, T_{ini} increased significantly from 334.0 to 367.0 °C, $T_{50\%}$ increased from 386.3 to 421.5 °C (Table 3); which are 33.0 and 35.2 °C higher than those of

Table 2
TGA characteristics of the measured samples under nitrogen atmosphere.

Composition	T_{ini} (°C) N_2	$T_{-50\%}$ (°C)	Residue at 700 °C (%)
Pure HDPE	416.5	456.0	0.5
5.0 wt% NPs	411.0	458.0	5.3
10.0 wt% NPs	415.5	462.5	10.3
15.0 wt% NPs	425.0	467.5	13.8
20.0 wt% NPs	432.0	469.0	18.5

Table 3
TGA characteristics of the measured samples under air atmosphere.

Composition	T_{ini} (°C)	$T_{-50\%}$ (°C)	Residue at 700 °C (%)
Pure HDPE	334.0	386.3	0.6
5.0 wt% NPs	367.0	421.5	7.0
10.0 wt% NPs	370.5	425.0	10.4
15.0 wt% NPs	382.5	435.5	19.1
20.0 wt% NPs	378.5	440.5	24.3

HDPE. Moreover, T_{ini} and $T_{50\%}$ further increased to 378.5 and 440.5 °C when the particle loading increased from 5.0 to 20.0 wt%, Table 3. The oxidative residues of theses PNCs at 700 °C are 7.0, 10.4, 19.1, and 24.3% for the PNCs with a particle loading of 5.0, 10.0, 15.0 and 20.0 wt%, respectively. Apparently, the significant increase in T_{ini}, $T_{50\%}$ and final residues with increasing particle loading indicate that the iron NPs deferred the HDPE matrix from oxidative decomposition at high temperatures through competitive reaction with oxygen. Hence, these NPs have effectively prevented oxygen from reaction with polymer hydrocarbon chains; which is the primary reason for the weight loss of polymeric materials under intensive heating under air. Thus, the thermal oxidative stability of the HDPE PNCs was significantly enhanced in the presence of iron NPs and further enhanced by increasing the particle loadings.

3.7. Melt rheological behaviors

The melt rheological behaviors of pure HDPE and its PNCs at 200 °C were investigated by studying the complex viscosity (η^*), storage moduli (G′, value of the stored energy which represents the elastic portion) and loss moduli (G″, value of energy dissipated as heat which represents the viscous portion) as a function of oscillation frequency (Hz). A 'percolation threshold' is defined as a critical concentration of nano-fillers, at which almost all the physical properties of the PNCs experience a sharp change [22]. Fig. 8a depicts the complex viscosity of pure HDPE and its PNCs as a function of oscillation frequency.

Both pure HDPE and all these PNCs exhibited a decreased η^* with the frequency increased from 0.1 to 100 Hz, which showed a typical shear thinning behavior [45,63]. For all these HDPE PNCs, η^* increased significantly with the incorporation of the iron NPs in the low frequency range from 0.1 to 0.4 Hz. This suggests that the mobility of HDPE molecule chains near the NPs were restrained [64]; and the contact probability between the HDPE chains and the NPs increased with increasing the particle loading, which in turn increased the complex viscosity of the HDPE matrix. Moreover, the aggregation of NPs can also hinder the movement of the HDPE chains and increase the complex viscosity. Similar results were also reported in HDPE/octamethyl-POSS [57] and HDPE/silicate systems [64].

The G′ and G″ as a function of oscillation frequency are shown in Fig. 8b and c, respectively. For both HDPE and its PNCs, G′ was widely separated in the low frequency range while it was only slightly separated in the high frequency range. This phenomena are due to the increased solid-like properties of the polymeric matrix if the oscillation frequency is enough low for the NPs to restrict the mobility of polymer chain [64]. Similar phenomena were also observed in the HDPE/POSS [57], HDPE/silicate [64] and HDPE/clay PNCs [65]. At low frequency (0.1–1.0 Hz), G′ increased significantly with 5.0 wt% particle loading; and G′ further increased accordingly with increasing the particle loading. In addition, a percolation plateau formed at 0.1–1.0 Hz frequency range is observed when the particle loading higher than 5.0 wt%, Fig. 8b. This "plateau" is due to either an inter-connected structure of the NPs or a strong particle-polymer interaction [22,66]. Since it has already been

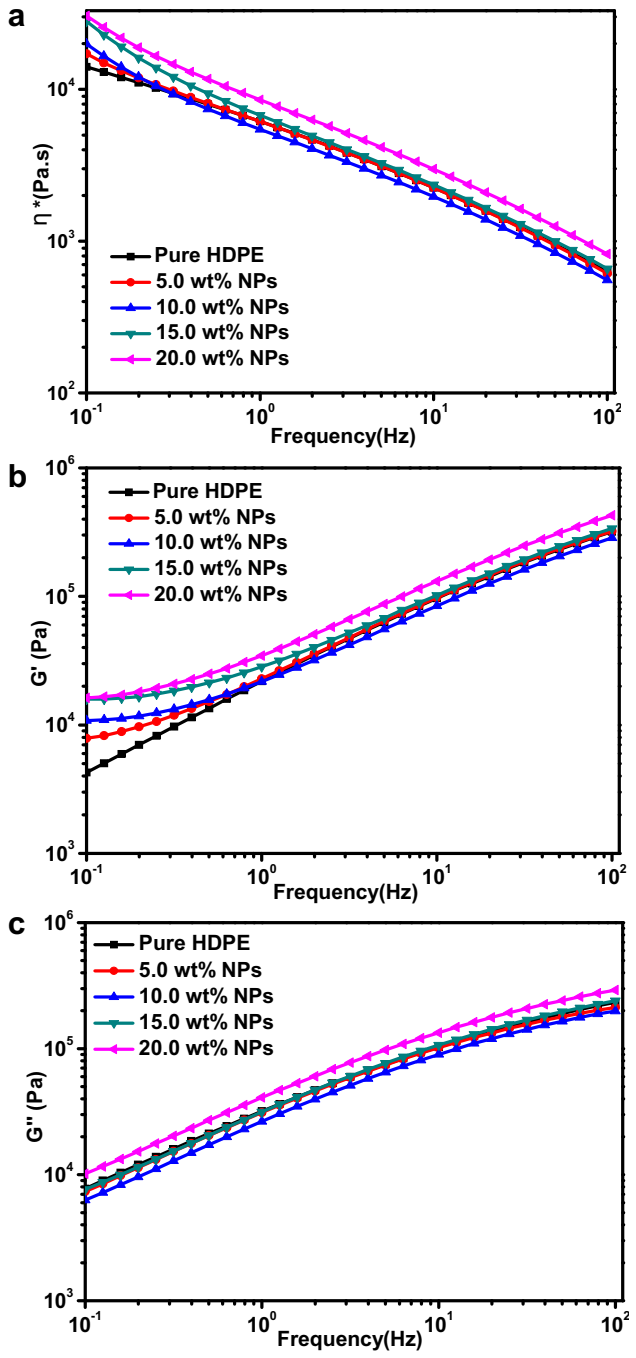

Fig. 8. Melt rheological properties (a) complex viscosity, (b) storage modulus, and (c) loss modulus of HDPE and its nanocomposites with different particle loadings.

known that the particle-polymer interaction here is mostly due to weak van der waals forces; thus, this percolation plateau is caused by the formation of inter-connected structure, which is consistent with TEM observations, Fig. 2. G″ was slightly changed between HDPE and its PNCs, which indicated that the energy dissipation effect is not significantly influenced after the addition of iron/iron oxide NPs.

3.8. Magnetic property

Fig. 9 shows the room temperature magnetic hysteresis loops of HDPE PNCs with different particle loadings. Table 4 gives the

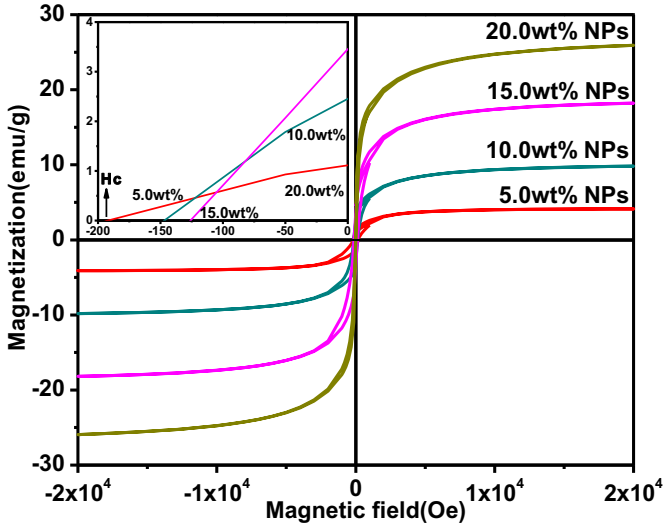

Fig. 9. Room temperature magnetic hysteresis loops of the HDPE nanocomposites with different particle loadings.

summary of the magnetic parameters. The insert of Fig. 9 shows the coercivity (coercive force, H_c) of the HDPE PNCs. H_c is defined as the applied external magnetic field, which is necessary to return one material to a zero magnetization condition. Saturation magnetization (M_s) is defined as the state, at which the magnetization of one material cannot be further increased with an increase of the external magnetic field. For all the samples tested, M_s is not reached even at a magnetic field of 2 T. M_s is thus determined by the extrapolation of the obtained M_s from the intercept of the magnetization versus the reverse of field (H^{-1}) at high magnetic field [35,67,68]. For HDPE PNCs, M_s increased significantly from 4.3 to 26.9 emu/g (Table 4) when the particle loading increased from 5.0 to 20.0 wt%. The M_s of bulk iron and γ-Fe_2O_3 are approximately 220 and 74 emu/g [69,70], respectively. According to the Mössbauer spectra results (18% iron and 72% Fe^{3+}), the theoretical M_s of HDPE PNCs with 5.0 wt% particle loading are the addition of M_s from both metallic iron and Fe_2O_3 ($220 \times 18\% + 74 \times 72\% = 92.9$ emu/g); which matches the measured M_s of 89.6 emu/g [$4.3 \times 100/(5.3 - 0.5) = 89.6$] very well and a standard deviation of ~2.3. However, the measured and theoretical M_s of HDPE PNCs with 20.0 wt% particle loading are 149.4 and 176.8 emu/g, respectively. The reasons of these lower measured M_s are attributed to partial oxidation of the iron NPs in HDPE matrix caused by the loss of net magnetic moment in the antiferromagnetic or ferrimagnetic oxide shell [71] (which are confirmed from Mössbauer spectra analysis) and interfacial behaviors between NPs and HDPE molecules [72,73]. From Table 4, it is obvious that all the tested samples have H_c lower than 200 Oe, indicating a soft ferromagnetic behavior of all the HDPE PNCs at room temperature. H_c is observed to decrease significantly with increasing the particle loading. Compared with the high H_c (192.9 Oe) of 5 wt% loading PNC, the much smaller H_c (8.8 Oe) in the 20 wt% loading HDPE PNCs is caused by the

Table 4
Magnetic properties of the measured samples.

Samples	M_s (emu/g)	H_c (Oe)
5.0 wt% NPs	4.3	192.9
10.0 wt% NPs	10.2	147.1
15.0 wt% NPs	18.9	125.8
20.0 wt% NPs	26.9	8.8

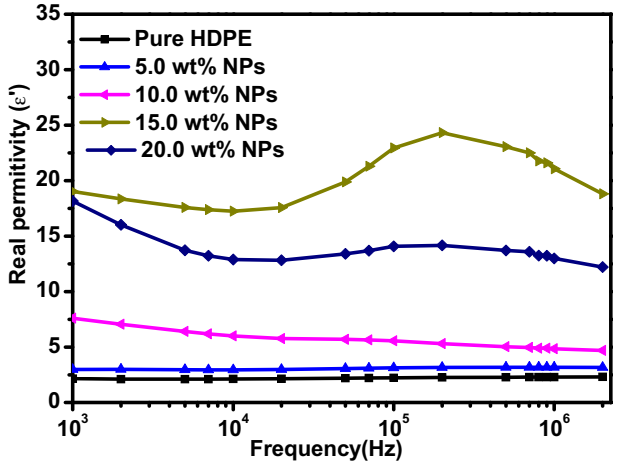

Fig. 10. Real permittivity of HDPE and its nanocomposites with different particle loadings.

decreased inter-particle distance concomitant with a stronger dipolar interaction [74]. This kind of particle-loading-dependent coercivity in nano-particle assembly was also observed in the iron NPs reinforced polyurethane [10] and iron oxide NPs reinforced vinyl-ester resin PNCs [74].

3.9. Dielectric property

Fig. 10 shows the real permittivity (ε') as a function of the frequency for pure HDPE and its PNCs at different particle loadings at room temperature. The pristine HDPE and the PNCs with 5.0 wt% particle loading are observed to have a constant ε' in all the frequency range, and the ε' values are similar to each other. In the case of HDPE PNCs with a 10.0 wt% particle loading, the ε' value slightly decreased with increasing oscillation frequency, which indicated a dielectric relaxation behavior [22]. The ε' value was observed to be significantly enhanced in the PNCs with a particle loading of 15.0 and 20.0 wt% and the ε' value fluctuated with increasing oscillation frequency, which indicates that the insulating layer is unstable and can be easily affected by the increased frequency. The probable reason is: after the presence of high amount NPs (~10.0 wt%), the insulating HDPE layers which were "physically wrapped" on the surface of NPs became thinner and not enough to hold the charge carriers of the iron NPs. This also explains the observed lower ε' value in HDPE PNCs with 20.0 wt% particle loading than that of HDPE NCs with 15.0 wt% particle loading.

4. Conclusion

The inert hydrocarbon-chain based HDPE has been introduced with magnetic property through a facile, surfactant-free, low-cost method; specifically, an in-situ thermal decomposition of organo-metallic precursor ($Fe(CO)_5$) in HDPE/xylene solution. TEM observations showed that the in-situ synthesized NPs were well dispersed in the HDPE matrix, and inter-network structure was formed when the particle loading reached 10.0 wt% due to the magnetic dipolar-dipolar interactions. FT-IR, XRD and DSC confirmed that there is no crystalline structure change of the HDPE during the synthesis of the HDPE PNCs. However, the heat of fusion and the crystalline fraction were decreased in the presence of the synthesized NPs because the NPs suppressed the crystallization. Mössbauer spectra indicated that the oxidation of the iron NPs was inhibited with increasing particle loading. Complex viscosity was increased and the storage modulus was enhanced for all these HDPE PNCs. A rheological plateau was formed at low oscillation frequency due to the inter-network structure of the as-synthesized NPs in the hosting HDPE matrix. Saturation magnetization was enhanced and coercivity was decreased by increasing the particle loading and all these PNCs behaved as soft ferromagnetic at room temperature. Thermal oxidative stability of the HDPE PNCs was significantly enhanced by the reaction between iron NPs and oxygen at accelerated oxidation temperatures. The real permittivity value of the HDPE PNCs with high particle loading (15.0, 20.0 wt%) indicated that the insulating HDPE layer became thinner and unstable to hold the charge carriers of the Fe NPs.

Acknowledgment

This project is supported by the Research Enhancement Grant from Lamar University. Partial financial support from National Science Foundation – Chemical and Biological Separations (CBET: 11-37441) managed by Dr. Rosemarie D. Wesson is appreciated. We also appreciate the support from National Science Foundation Nanoscale Interdisciplinary Research Team and Materials Processing and Manufacturing (CMMI 10-30755) to purchase TGA and DSC. D. P. Young acknowledges support from the NSF under Grant No. DMR 10-05764.

References

[1] Khanna S, Linderoth S. Phys Rev Lett 1991;67(6):742–5.
[2] Farrell D, Majetich SA, Wilcoxon JP. J Phys Chem B 2003;107(40):11022–30.
[3] Lin X, Sorensen C, Klabunde K, Hadjipanayis G. Langmuir 1998;14(25):7140–6.
[4] Petit C, Taleb A, Pileni M. J Phys Chem B 1999;103(11):1805–10.
[5] Apsel S, Emmert J, Deng J, Bloomfield L. Phys Rev Lett 1996;76(9):1441–4.
[6] Ely TO, Amiens C, Chaudret B, Snoeck E, Verelst M, Respaud M, et al. Chem Mater 1999;11(3):526–9.
[7] Hsieh TH, Ho KS, Bi X, Han YK, Chen ZL, Hsu CH, et al. Eur Polym J 2009;45(3):613–20.
[8] Nathani H, Misra R. Mater Sci Eng B 2004;113(3):228–35.
[9] Guo Z, Lee SE, Kim H, Park S, Hahn H, Karki A, et al. Acta Mater 2009;57(1):267–77.
[10] Guo Z, Park S, Hahn HT, Wei S, Moldovan M, Karki AB, et al. J Appl Phys 2007;101:09M511.
[11] Guo Z, Park S, Wei S, Pereira T, Moldovan M, Karki AB, et al. Nanotechnology 2007;18:335704.
[12] Zhu J, Wei S, Zhang L, Mao Y, Ryu J, Mavinakuli P, et al. J Phys Chem C 2010;114(39):16335–42.
[13] Zhu J, Wei S, Zhang L, Mao Y, Ryu J, Karki AB, et al. J Mater Chem 2010;21(2):342–8.
[14] Zhu J, Wei S, Zhang L, Mao Y, Ryu J, Haldolaarachchige N, et al. J Mater Chem 2011;21:3952–9.
[15] Zhu J, Wei S, Rutman D, Haldolaarachchige N, Young DP, Guo Z. Polymer 2011;52:2947–55.
[16] Wei S, Patil R, Sun L, Haldolaarachchige N, Chen X, Young DP, et al. Macromol Mater Eng 2011;296:850–7.
[17] Chen X, Wei S, Gunesoglu C, Zhu J, Southworth CS, Sun L, et al. Macromol Chem Phys 2010;211(16):1775–83.
[18] Nathani H, Gubbala S, Misra R. Mater Sci Eng B 2004;111(2–3):95–100.
[19] Ohlan A, Singh K, Chandra A, Dhawan SK. ACS Appl Mater Interfaces 2010;2(3):927–33.
[20] Zhu J, Wei S, Ryu J, Sun L, Luo Z, Guo Z. ACS Appl Mater Interfaces 2010;2:2100–7.
[21] Mu S, Wu D, Wang Y, Wu Z, Yang X, Yang W. ACS Appl Mater Interfaces 2009;2(1):111–8.
[22] Zhu J, Wei S, Li Y, Sun L, Haldolaarachchige N, Young DP, et al. Macromolecules 2011;44:4382–91.
[23] Zhu J, Wei S, Ryu J, Budhathoki M, Liang G, Guo Z. J Mater Chem 2010;20(23):4937–48.
[24] Guo Z, Kim TY, Lei K, Pereira T, Sugar JG, Hahn HT. Compos Sci Technol 2008;68(1):164–70.
[25] Ziolo RF, Giannelis EP, Weinstein BA, O'Horo MP, Ganguly BN, Mehrotra V, et al. Science 1992;257(5067):219–23.
[26] Zhu J, Wei S, Alexander M, Dang TD, Ho TC, Guo Z. Adv Funct Mater 2010;20(18):3076–84.
[27] Dai Q, Berman D, Virwani K, Frommer J, Jubert PO, Lam M, et al. Nano Lett 2010;10:3216–21.

[28] Kim P, Doss NM, Tillotson JP, Hotchkiss PJ, Pan MJ, Marder SR, et al. ACS Nano 2009;3(9):2581–92.
[29] Shimada T, Ookubo K, Komuro N, Shimizu T, Uehara N. Langmuir 2007; 23(22):11225–32.
[30] Urbina MC, Zinoveva S, Miller T, Sabliov CM, Monroe WT, Kumar CSSR. J Phys Chem C 2008;112(30):11102–8.
[31] Wei S, Wang Q, Zhu J, Sun L, Lin H, Guo Z. Nanoscale 2011;3(11):4474–502.
[32] Guo Z, Moldovan M, Young DP, Henry LL, Podlaha EJ. Electrochem Solid-State Lett 2007;10:E31–5.
[33] Burke NAD, Stöver HDH, Dawson FP. Chem Mater 2002;14(11):4752–61.
[34] Wizel S, Margel S, Gedanken A. Polym Int 2000;49(5):445–8.
[35] Guo Z, Henry LL, Palshin V, Podlaha EJ. J Mater Chem 2006;16(18):1772–7.
[36] Hou Y, Yu J, Gao S. J Mater Chem 2003;13(8):1983–7.
[37] Tannenbaum R, Zubris M, Goldberg EP, Reich S, Dan N. Macromolecules 2005; 38(10):4254–9.
[38] Grigoriadou I, Paraskevopoulos K, Chrissafis K, Pavlidou E, Stamkopoulos TG, Bikiaris D. Polym Degrad Stab 2010;96:151–63.
[39] Tanniru M, Yuan Q, Misra R. Polymer 2006;47(6):2133–46.
[40] Jeon K, Lumata L, Tokumoto T, Steven E, Brooks J, Alamo RG. Polymer 2007; 48(16):4751–64.
[41] Gilmer TC, Williams M. J Chem Educ 1996;73(11):1062–5.
[42] Kim J, Kwak S, Hong SM, Lee JR, Takahara A, Seo Y. Macromolecules 2010;43: 10545–53.
[43] Thongruang W, Spontak RJ, Balik CM. Polymer 2002;43(8):2279–86.
[44] Yang BX, Pramoda KP, Xu GQ, Goh SH. Adv Funct Mater 2010;20(18): 3076–84. 2007;17(13):2062-2069.
[45] Kim J, Hong SM, Kwak S, Seo Y. Phys Chem Chem Phys 2009;11(46):10851–9.
[46] Schonhals A, Goering H, Costa FR, Wagenknecht U, Heinrich G. Macromolecules 2009;42(12):4165–74.
[47] Giri AK. J Appl Phys 1997;81:1348–50.
[48] Smith TW, Wychick D. J Phys Chem 1980;84(12):1621–9.
[49] Wonterghem J, Mørup S, Charles SW, Wells S, Villadsen J. Phys Rev Lett 1985; 55(4):410–3.
[50] Uhm YR, Kim J, Lee S, Jeon J, Rhee CK. Ind Eng Chem Res 2011;50:4478–83.
[51] Li L, Li G, Smith R, Inomata H. Chem Mater 2000;12(12):3705–14.
[52] Battisha I, Afify H, Ibrahim M. J Magn Magn Mater 2006;306(2):211–7.
[53] Inci B, Wagener KB. J Am Chem Soc 2011;133(31):11872–5.
[54] Trujillo M, Arnal M, Müller A, Laredo E, Bredeau St, Bonduel D, et al. Macromolecules 2007;40(17):6268–76.
[55] Waddon A, Zheng L, Farris R, Coughlin EB. Nano Lett 2002;2(10):1149–55.
[56] Butler MF, Donald AM, Bras W, Mant GR, Derbyshire GE, Ryan AJ. Macromolecules 1995;28(19):6383–93.
[57] Joshi M, Butola B, Simon G, Kukaleva N. Macromolecules 2006;39(5): 1839–49.
[58] Li S, Wu P, Li H, Zhu N, Li P, Wu J, et al. Appl Clay Sci 2010;50(3):330–6.
[59] Wunderlich B, Czornyj G. Macromolecules 1977;10(5):906–13.
[60] Yang J, Wang C, Wang K, Zhang Q, Chen F, Du R, et al. Macromolecules 2009; 42(18):7016–23.
[61] Kodjie SL, Li L, Li B, Cai W, Li CY, Keating M. J Macromol Sci B 2006;45(2): 231–45.
[62] Barus S, Zanetti M, Lazzari M, Costa L. Polymer 2009;50(12):2595–600.
[63] Wood-Adams PM, Dealy JM, Willem deGroot A, Redwine OD. Macromolecules 2000;33(20):7489–99.
[64] Chae DW, Kim KJ, Kim BC. Polymer 2006;47(10):3609–15.
[65] Swain SK, Isayev AI. Polymer 2007;48(1):281–9.
[66] Pötschke P, Abdel-Goad M, Alig I, Dudkin S, Lellinger D. Polymer 2004;45(26): 8863–70.
[67] Chen J, Sorensen C, Klabunde K, Hadjipanayis G. J Appl Phys 1994;76(10): 6316–8.
[68] Zhang D, Klabunde K, Sorensen C, Hadjipanayis G. Phys Rev B 1998;58(21): 14167–70.
[69] Peng S, Wang C, Xie J, Sun S. J Am Chem Soc 2006;128(33):10676–7.
[70] Rao PM, Zheng X. Nano Lett 2011;11(6):2390–5.
[71] Leslie-Pelecky DL, Rieke RD. Chem Mater 1996;8(8):1770–83.
[72] Zhang D, Chung R, Karki AB, Li F, Young DP, Guo Z. J Phys Chem C 2009;114(1): 212–9.
[73] Guo Z, Park S, Hahn HT, Wei S, Moldovan M, Karki AB, et al. Appl Phys Lett 2007;90:053111.
[74] Guo Z, Lei K, Li Y, Ng HW, Prikhodko S, Hahn HT. Compos Sci Technol 2008; 68(6):1513–20.